Construction and Building Materials 162 (2018) 584–595

Contents lists available at ScienceDirect

Construction and Building Materials

journal homepage: www.elsevier.com/locate/conbuildmat

Reduced-scale experiments to evaluate performance of composite building envelopes containing phase change materials

Benjamin A. Young [a], Gabriel Falzone [b], Zhenhua Wei [b], Gaurav Sant [b,c], Laurent Pilon [a,*]

[a] Mechanical and Aerospace Engineering Department, Henry Samueli School of Engineering and Applied Science, University of California, Los Angeles, United States
[b] Civil and Environmental Engineering Department, Henry Samueli School of Engineering and Applied Science, University of California, Los Angeles, United States
[c] California Nanosystems Institute (CNSI), Henry Samueli School of Engineering and Applied Science, University of California, Los Angeles, United States

HIGHLIGHTS

- A new method is proposed to rapidly assess building envelope thermal performance.
- It was based on scaling analysis to design reduced-scale models of actual buildings.
- It was applied to PCM-composite envelopes than can reduce/delay building energy use.
- The new method requires less material, time, and space than previous studies.

ARTICLE INFO

Article history:
Received 7 July 2017
Accepted 29 November 2017

Keywords:
Phase change materials
Building envelopes
Scaling analysis
Energy efficiency

ABSTRACT

This study presents a convenient approach to rapidly assess the thermal performance of building envelopes containing phase change materials (PCMs) or other building materials. It establishes that the transient thermal behavior of full-scale building test structures featuring envelopes with PCMs can be represented by a reduced-scale test cell conveniently placed inside an environmental chamber. Indeed, PCM-composite envelopes have been considered for reducing and time-shifting the thermal load on buildings thanks to the latent heat associated with reversible transition between liquid and solid phases. First, a thermal model coupling outdoor, wall, and indoor temperatures and accounting for PCM latent heat was developed. It was validated against experimental temperature measurements within a reduced-scale test cell enclosure placed in an environmental chamber and subjected to a series of sinusoidal temperature cycles. Then, scaling analysis of the experimentally-validated thermal model was performed. It identified eight dimensionless numbers governing the transient thermal behavior of building structures with envelopes containing PCMs. The scaling analysis was validated using detailed numerical simulations for different enclosure geometries and outside diurnal climate conditions. Finally, the method was demonstrated on full-scale experiments reported in the literature. It can be used to assess building envelope thermal performance by designing representative reduced-scale experiments without requiring a significant amount of material, time, or space.

1. Introduction

Residential and commercial buildings accounted for 41% of primary energy consumption in the United States in 2015 [1]. Heating, ventilation, and air-conditioning (HVAC) systems are responsible for about half of the energy consumption in buildings [1]. Composite building envelopes containing microencapsulated phase change materials (PCMs) have received attention as a means of reducing space heating/cooling energy consumption [2–5]. Indeed, PCMs store large amounts of thermal energy in the form of latent heat associated with reversible liquid/solid phase change(s). Such latent heat storage increases the thermal mass of the building envelope. This can result in (i) a decrease in a building's heating and cooling loads and (ii) a time-shift of a building's heating and cooling loads to take advantage of time-of-use (TOU) electricity pricing. Such actions reduce energy costs for ratepayers and capital costs for peaker plants operated by utilities [2–6].

Several experimental studies [7–12] have investigated the effect of PCM embedded in cementitious building envelope materials on the thermal behavior of full-scale test enclosures subjected

* Corresponding author at: Engineering IV, 420 Westwood Plaza, Los Angeles, CA 90095-1597, United States.
E-mail address: pilon@seas.ucla.edu (L. Pilon).

https://doi.org/10.1016/j.conbuildmat.2017.11.160
0950-0618/

Nomenclature

Bi	Biot number
c_p	specific heat, J/(kg K)
C_r	heat capacity ratio
Fo	Fourier number
h	convective heat transfer coefficient, W/(m^2 K)
h_{sf}	latent heat of fusion, kJ/kg
k	thermal conductivity, W/(m K)
L	wall thickness, m
q''	heat flux, W/m^2
t	time, s or h
$T_a(t)$	inside air temperature, °C
$T_o(t)$	outside/chamber temperature, °C
$T_w(x,t)$	wall temperature, °C
$T_{o,max}, T_{o,min}$	maximum and minimum outside temperatures, °C
T_{pc}	PCM melting temperature, °C
x	spatial coordinate, m
w/c	water/cement ratio

Greek symbols

α	thermal diffusivity, m^2/s
ΔT_{pc}	PCM melting temperature window, °C
ϕ_j	volume fraction of material "j" in composite
ρ	density, kg/m^3
τ	oscillation period, h

Subscripts

a	refers to air
c	refers to core material in composite
$c+s$	refers to core–shell microcapsule
eff	refers to effective properties
l	refers to liquid phase
m	refers to matrix material in composite
q	refers to quartz
s	refers to solid phase or shell material in composite

Superscripts

$*$	refers to dimensionless quantity

to natural outdoor climates, for example, in southern Spain [7] or the continental United States [9]. These studies have demonstrated the ability of PCMs to reduce the magnitude of interior temperature fluctuations and/or to decrease the amount of energy required for space conditioning [7–10,12]. While insightful and comprehensive, such experimental efforts are highly cost, time, and resource intensive. For example, it is time-consuming to build such enclosures and to collect data over periods of days or months.

To overcome such challenges without sacrificing the quality and nature of insights obtained, the present study demonstrates how scaling analysis can be used to extend the results of a reduced-scale experimental test cell placed within an environmental chamber to full-scale experimental enclosures analogous to real buildings. Such scaling analysis permits rapid, accurate parametric investigations of the ability of PCMs or of other approaches to reduce and delay space conditioning (HVAC) energy needs within energy-efficient buildings.

2. Background

2.1. Previous experimental studies

Numerous experimental studies have been conducted to compare the thermal behavior of test rooms with and without PCM-composite envelopes. Cabeza et al. [7] constructed a pair of large outdoor cubicles (2 m × 2 m × 3 m) with a conventional concrete envelope or with a composite concrete envelope containing 5 wt % microencapsulated PCM with a melting temperature around 26 °C in the south, west, and roof walls. The cubicles were subjected to the climate of Puigverd de Lleida, Spain over a period of three summer months. The authors found that the cubicle containing PCM featured smaller interior wall temperature fluctuations and smaller inner wall heat flux (heat load). Castell et al. [8] performed similar experiments on concrete and alveolar brick cubicles with and without macroencapsulated PCM. Here, the authors included an active cooling system within the cubicles. They found that the inclusion of PCM decreased the cooling energy requirement by about 15% over a summer season.

Zhang et al. [9] constructed two 1.83 m × 1.83 m × 1.22 m test rooms featuring wooden frame walls without and with PCM featuring a melting temperature window between 20 °C and 30 °C. The PCM was macroencapsulated in copper tubes embedded in the insulation layer of the wall. The test rooms were exposed to summer conditions in Lawrence, Kansas, and the indoor temperature of the test rooms was controlled by an air conditioning system. The authors found that the space cooling energy requirement for a summer day was reduced by 8.6% for a wall with 10% PCM by weight and by 10.8% for a wall with 20% PCM by weight.

Kuznik and Virgone [10] constructed an experimental setup consisting of a large test room (3.1 m × 3.1 m × 2.5 m) adjacent to a climatic chamber on one side. An array of heat lamps was also used to simulate incident solar radiation. The outdoor temperature and solar radiation flux corresponding to a summer, mid-season, and a winter day were imposed at the outer surface of the test room wall. The authors found that when the test room walls were modified to include an additional 5 mm-thick wallboard layer with 60 wt% microencapsulated PCM with melting temperature around 20 °C, the amplitude of the indoor temperature oscillation was reduced by 21–27% for all days simulated. They also found that the maximum indoor temperature was reduced by up to 4 °C in the summer.

Fang and Zhang [11] constructed three test cells with dimensions 0.7 m × 0.7 m × 0.7 m. Each test cell had five ordinary gypsum board walls and a ceiling wall containing either 0, 20, or 50 wt% of impregnated PCM with a melting temperature around 23 °C. The authors used a tungsten heat lamp placed at various vertical distances above the top wall to simulate solar radiation. In the experiments, the lamp was switched on and the resulting transient change in the interior test cell temperature was recorded. The maximum temperature attained by the interior air was reduced by 5°C and 9 °C for wall panels containing 20 wt% and 50 wt% of PCM, respectively. Note that the authors did not measure the response of the test cells to periodic exterior temperature fluctuations.

Overall, previous experimental studies of diurnal thermal response of building enclosures with envelopes made of PCM-composite walls have been limited to full-scale test rooms placed in various actual or simulated outdoor climates. Unfortunately, such experiments are time-consuming and resource-intensive to build, operate, and optimize. The objective of the present study is to demonstrate that a reduced-scale test cell subjected to faster

temperature fluctuations in a controlled environmental chamber can be used in place of a full-scale outdoor setup.

2.2. Numerical modeling of PCM-composite walls

The microencapsulated PCM-composite wall material considered in this study was a heterogeneous composite material consisting of spherical PCM (core–shell) microcapsules randomly dispersed in a mortar matrix. Previously, we demonstrated that the transient thermal response of such a composite is equivalent to that of a homogeneous material with some effective thermal properties [6,13,14]. The effective thermal conductivity k_{eff} of this three-component system was accurately predicted by the Felske model [15]. The effective volumetric heat capacity $(\rho c_p)_{eff}$ was given as the weighted sum of the individual components' heat capacity [6]. This approach significantly reduces the computational effort needed to solve for the temperature distribution within the wall, compared with that required to simulate a heterogeneous material with 3D geometry. Additionally, one must also account for the temperature-dependent specific heat $c_{p,c}(T)$ of the PCM. It can be determined experimentally by differential scanning calorimetry (DSC) [16]. Alternatively, the effective heat capacity method can be used to approximate $c_{p,c}(T)$ as a simple piecewise function of temperature [17] featuring a melting temperature window of width ΔT_{pc} centered around the melting temperature T_{pc} such that [17],

$$c_{p,c}(T) = \begin{cases} c_{p,c,s} & \text{for} \quad T < T_{pc} - \Delta T_{pc}/2 \\ c_{p,c,s} + \frac{h_{sf}}{\Delta T_{pc}} & \text{for} \quad T_{pc} - \Delta T_{pc}/2 \leqslant T \leqslant T_{pc} + \Delta T_{pc}/2 \\ c_{p,c,l} & \text{for} \quad T > T_{pc} + \Delta T_{pc}/2 \end{cases} \tag{1}$$

where $c_{p,c,s}$ and $c_{p,c,l}$ are the specific heats of the PCM in the solid and liquid phases, respectively, while h_{sf} is the latent heat of fusion (in J/kg). The effective heat capacity method has been shown to provide temperature predictions in PCM-composites similar to those obtained using actual DSC data or a Gaussian-shaped approximation of $c_{p,c}(T)$ [18]. It also allows one to easily parametrize different PCM properties such as h_{sf} or ΔT_{pc}.

3. Materials and methods

3.1. Experimental setup

Two concrete wall panels 45 cm in length and width and 2.54 cm in thickness were fabricated for this study, namely (i) a plain mortar wall panel consisting of 45% cement paste and 55% quartz inclusions by volume and (ii) a PCM-composite wall panel consisting of 45% cement paste, 45% quartz, and 10% microencapsulated PCM by volume (MPCM24D, Microtek Laboratories, Inc.). The PCM microcapsules consisted of a paraffin-based core material enclosed in a melamine-formaldehyde (MF) shell. The melting temperature T_{pc} of the PCM was around 24 °C and the latent heat of fusion was 160 kJ/kg [18].

The wall panels were fabricated using commercially available Type I/II ordinary portland cement and deionized (DI) water. For the PCM-composite panel, the desired microencapsulated PCM volume fraction $\phi_{c+s} = 0.1$ was achieved by measuring and adding the appropriate mass based on the density of the PCM microcapsules ρ_{c+s} taken as 900 kg/m^3 [19]. The mortars were prepared according to ASTMC305 [20], and the water-to-cement (w/c) ratio on a mass basis was 0.45. A commercial viscosity-modifying admixture (MasterMatrix VMA 450, BASF Corporation) was added at 0.1% of the total mortar mass to minimize segregation of inclusions and maintain a homogeneous distribution of PCM microcapsules and quartz inclusions in the specimen. An acrylic plastic mold was used to fabricate the wall panels with the desired dimensions. The wall panels were allowed to cure in sealed conditions for 28 days.

Fig. 1a shows a photograph of the experimental cubic test cell of length 45 cm. The base and four side walls of the cell were made of

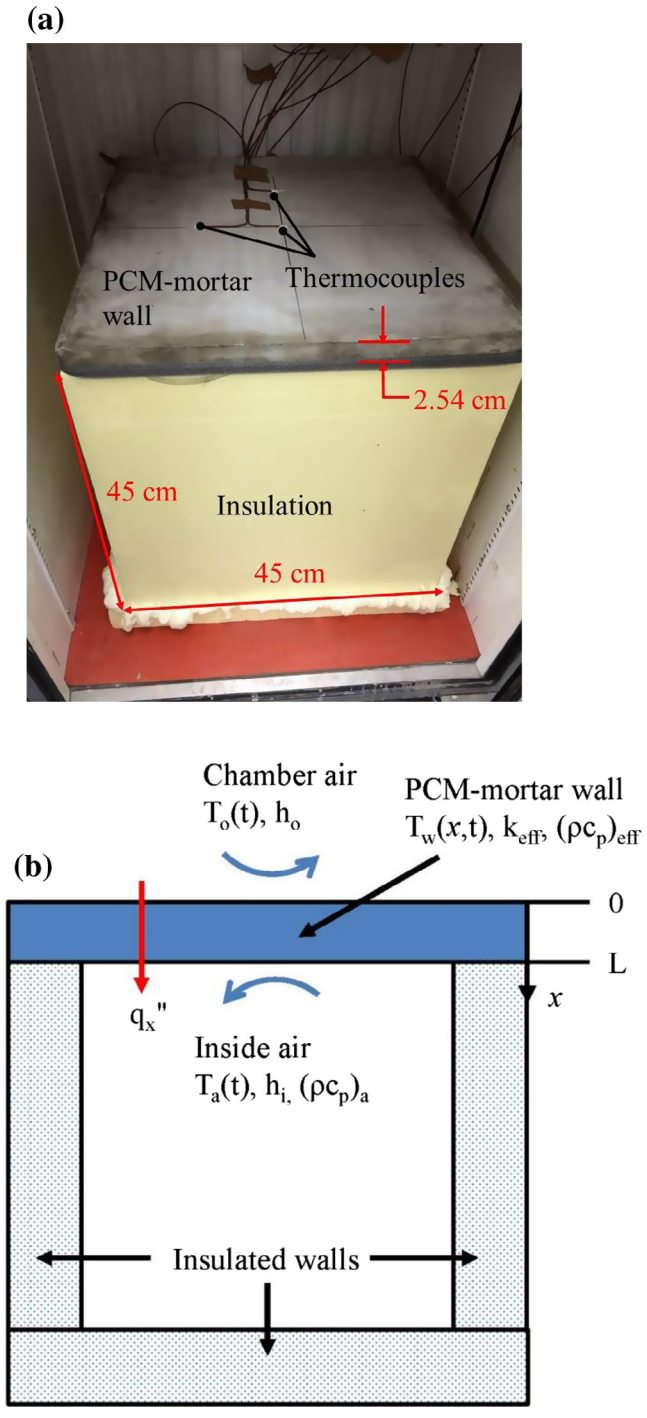

Fig. 1. (a) Photograph of the experimental test cell with dimensions of 45 cm × 45 cm × 45 cm. Five walls were made of 5.08 cm thick foam insulation while the remaining face was made of a plain mortar or PCM-mortar composite wall panel 2.54 cm in thickness. Thermocouples were placed at three different lateral locations on the inner and outer wall surfaces and at four different locations inside the test cell. (b) Schematic of a test cell with a single PCM-composite wall and five insulated walls placed inside an environmental test chamber. The wall has effective thermal properties k_{eff} and $(\rho c_p)_{eff}$. Both the outer ($x = 0$) and inner ($x = L$) wall surfaces are exposed to convection with the chamber and inside air, respectively.

5.08 cm (2 inch) thick CertiFoam® insulation with an R-value of 1.8 (m^2 K)/W (DiversiFoam Products, Inc.). The top wall was one of the concrete wall panels previously described. A total of 10 thermocouples were placed at four different locations within the test cell and at three different lateral locations on the inner and outer wall surfaces. To ensure that the interior air was well-mixed and had uniform temperature $T_a(t)$, a small computer fan with a blade diameter of 8 cm (EFX-08-12, SilenX Corporation) was placed inside the test cell and powered at its maximum speed of 1400 ± 210 rpm.

3.2. Experimental procedure

The test cell was placed in a programmable freeze–thaw environmental chamber (TH024, Darwin Chambers Company) and subjected to four different sinusoidal chamber temperature cycles of period τ = 1.5 h such that the chamber temperature $T_o(t)$ was,

$$T_o(t) = \left(\frac{T_{o,max} - T_{o,min}}{2}\right) \sin\left(\frac{2\pi t}{1.5}\right) + \frac{T_{o,max} + T_{o,min}}{2} \quad (2)$$

where t is in hours, while $T_{o,min}$ and $T_{o,max}$ are the minimum and maximum values of $T_o(t)$. The four cycles were defined to explore a wide range of outdoor temperature oscillations with respect to the PCM melting temperature T_{pc} = 24 °C: (i) Cycle A with $T_{o,min}$ = 5 °C, $T_{o,max}$ = 20 °C, (ii) Cycle B with $T_{o,min}$ = 15 °C, $T_{o,max}$ = 40 °C, (iii) Cycle C with $T_{o,min}$ = 10 °C, $T_{o,max}$ = 30 °C, and (iv) Cycle D with $T_{o,min}$ = 5 °C, $T_{o,max}$ = 35 °C.

During each experiment, the temperature inside the test cell $T_a(t)$ was recorded as a function of time. Additionally, the inner and outer wall surface temperatures were also recorded. Each experiment was run for at least 12 h in order to allow the system to reach a periodic steady state and to collect data for several oscillation periods. Experimental data from Cycle A was used to estimate the convective heat transfer coefficients prevailing in the environment chamber, as well as to verify periodic behavior of the inside air temperature. The other three cycles (B-D) were used to compare inside air temperature evolutions for test cells with either a plain mortar or PCM-mortar composite wall.

4. Analysis

4.1. Schematic and assumptions

Fig. 1b shows a schematic of the test cell with inside air temperature $T_a(t)$ with a PCM-mortar composite wall placed inside an environmental chamber with temperature $T_o(t)$ along with the associated coordinate system. The top mortar-based wall had thickness L and effective thermal properties $(\rho c_p)_{eff}(T)$ and k_{eff}. Convective heat transfer took place between the chamber air and the exterior wall surface at $x = 0$. Likewise, convective heat transfer also took place between the inside air and the interior surface of the wall at $x = L$. Heat was conducted through the wall in the x-direction, and the other walls of the cell were treated as perfectly thermally insulated.

To make the problem mathematically tractable, the following assumptions were made: (1) the inside air was assumed to be well-mixed with uniform indoor temperature $T_a(t)$, (2) heat generation within the test cell was ignored, (3) one-dimensional (1D) heat conduction normal to the wall surfaces prevailed, (4) all material properties were constant and isotropic except for the temperature-dependent specific heat $c_{p,c+s}(T)$ of the PCM, (5) the PCM specific heat in the solid and liquid phases was the same (i.e., $c_{p,c+s,s} = c_{p,c+s,l}$), and (6) all walls other than the mortar or PCM-composite wall were assumed to be perfectly insulated. To justify this final assumption, it was verified that the predicted inside air temperature $T_a(t)$ did not differ by more than 0.2 °C when heat transfer through the foam base and side walls was accounted for.

4.2. Governing equations

The temperature in the composite wall $T_w(x,t)$ was governed by the 1D transient heat diffusion equation [21],

$$\frac{\partial T_w}{\partial t} = \alpha_{eff}(T_w)\frac{\partial^2 T_w}{\partial x^2} \quad (3)$$

where $\alpha_{eff}(T) = k_{eff}/(\rho c_p)_{eff}(T)$ is the effective thermal diffusivity of the wall. Additionally, the energy conservation equation for the inside air can be expressed as,

$$(\rho c_p)_a V_a \frac{dT_a}{dt} = h_i A_w [T_w(L,t) - T_a(t)] \quad (4)$$

where V_a is the volume of air in the test cell, A_w is the surface area of the plain mortar or PCM-mortar wall and h_i is the convective heat transfer coefficient between the inner wall surface ($x = L$) and the inside air. Experimentally, these dimensions were $V_a = 0.04 m^3$, A_w = 0.12 m^2, and L = 2.54 cm.

4.3. Initial and boundary conditions

The inside air and the wall were assumed to have an initial uniform temperature T_i at t = 0, i.e.,

$$T_w(x,0) = T_a(0) = T_i. \quad (5)$$

Additionally, two convective heat flux boundary conditions for solving Eq. (3) were imposed at the inner ($x = L$) and outer ($x = 0$) wall surfaces so that

$$-k_{eff}\frac{\partial T_w}{\partial x}(0,t) = h_o[T_o(t) - T_w(0,t)] \quad \text{and}$$
$$-k_{eff}\frac{\partial T_w}{\partial x}(L,t) = h_i[T_w(L,t) - T_a(t)]. \quad (6)$$

Note that the governing Eqs. (3) and (4) are coupled by virtue of the fact that the convective heat flux at the inner wall surface ($x = L$) is dependent on both the inner wall surface temperature $T_w(L,t)$ and the inside air temperature $T_a(t)$.

4.4. Constitutive relationships

Table 1 summarizes the density ρ and specific heat c_p of cement paste, quartz, microencapsulated PCM (MPCM24D), and air used in the simulations. The effective volumetric heat capacity of the composite wall panel was predicted by a volume-weighted average as,

$$(\rho c_p)_{eff}(T) = \phi_{c+s}(\rho c_p)_{c+s}(T) + \phi_q(\rho c_p)_q + (1 - \phi_{c+s} - \phi_q)(\rho c_p)_m \quad (7)$$

where the subscripts $c+s, q$, and m refer to microencapsulated PCM, quartz, and cement paste, respectively. Fig. 2 plots the experimentally measured specific heat $c_{p,c+s}(T)$ of MPCM24D PCM microcapsules as a function of temperature for a ramp rate of 1°C/min, previously reported in [18]. Based on these measurements, the latent heat of fusion h_{sf} of the PCM was determined to be 160 kJ/kg. The multitude of peaks in the DSC curves can be attributed to the presence of impurities (i.e., constituents with different molecular weights) within the commercial PCM [18]. Note that $c_{p,c+s}(T)$ differs slightly depending on whether the sample is heated or cooled. Here, the data from the heating curve was used in Eq. (7) to simulate the experiments. Finally, the effective thermal conductivity k_{eff} of the mortar and PCM-composite wall panels was obtained from experimental measurements using the guarded hot-plate method

Table 1
Density ρ and specific heat c_p of cement paste, quartz, MPCM24D, and air.

Material	Subscript	ρ (kg/m^3)	c_p (J/(kg K))	Ref.
Cement paste	m	1965	1530	[28]
Quartz	q	2650	745	[21]
MPCM24D	c + s	900	$c_{p,c+s}(T)$	[18]
Air	a	1.2	1005	[21]

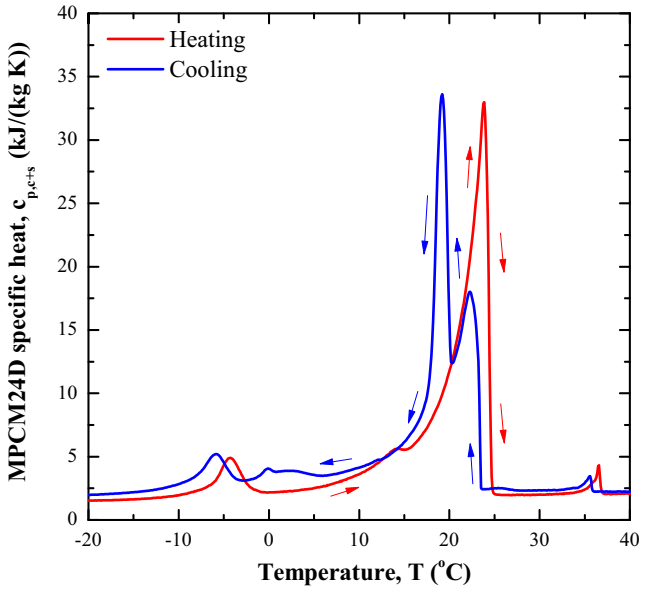

Fig. 2. Specific heat $c_{p,c+s}(T)$ of MPCM24D PCM microcapsules measured by DSC as a function of temperature with a temperature ramp rate of 1 °C/min [18]. The data from the heating curve was used to determine $(\rho c_p)_{eff}(T)$ for numerical simulations of the test cell experiments.

[14]. Here, k_{eff} was taken as 1.77 ± 0.27 W/(m K) for the plain mortar wall panel and as 1.46 ± 0.22 W/(m K) for the composite wall panel with 10 vol% of PCM where the experimental uncertainty represents one standard deviation [14].

4.5. Method of solution

The governing Eqs. (3) and (4) were solved along with the corresponding boundary and initial conditions using an explicit finite difference method. Convergence criteria was defined such that the inside air and wall temperature spatiotemporal evolutions differed by no more than 1% when the nodal spacing Δx or the time step Δt was reduced by a factor of 2. A numerically converged solution was achieved using a nodal spacing Δx = 2.5 mm and a time step Δt = 5 s. The finite element code used to solve the transient heat diffusion equation in the wall with phase change was validated against an exact solution of the Stefan problem for transient 1D heat conduction through a paraffin slab [13,22].

4.6. Scaling analysis

In order to non-dimensionalize the coupled governing Eqs. (3) and (4), the following dimensionless variables were introduced,

$$x^* = \frac{x}{L}, \quad t^* = Fo = \frac{\alpha_{eff,s} t}{L^2}, \quad T_w^*(x^*, t^*) = \frac{T_w(x,t) - T_{o,min}}{T_{o,max} - T_{o,min}},$$
$$T_a^*(t^*) = \frac{T_a(t) - T_{o,min}}{T_{o,max} - T_{o,min}}. \tag{8}$$

Here, $\alpha_{eff,s}$ is the effective thermal diffusivity of the wall based on the PCM solid phase specific heat $c_{p,c+s,s}$. Substituting Eqs. (8) into Eq. (3) yields,

$$\frac{1}{\alpha_{eff}^*(T_w^*)} \frac{\partial T_w^*}{\partial t^*} = \frac{\partial^2 T_w^*}{\partial x^{*2}}. \tag{9}$$

The dimensionless thermal diffusivity $\alpha_{eff}^*(T^*)$ can be expressed based on the effective heat capacity method and assuming $c_{p,c+s,s} = c_{p,c+s,l}$ [Assumption (5)] as,

$$\frac{1}{\alpha_{eff}^*(T^*)} = \frac{(\rho c_p)_{eff}(T)}{(\rho c_p)_{eff,s}}$$
$$= \begin{cases} 1 & \text{for} \quad T^* < T_{pc}^* - \Delta T_{pc}^*/2 \\ 1 + \frac{\phi_{c+s} h_{sf}^*}{\Delta T_{pc}^*} & \text{for} \quad T_{pc}^* - \Delta T_{pc}^*/2 \leqslant T^* \leqslant T_{pc}^* + \Delta T_{pc}^*/2 \\ 1 & \text{for} \quad T^* > T_{pc}^* + \Delta T_{pc}^*/2 \end{cases} \tag{10}$$

where the dimensionless PCM melting temperature T_{pc}^* and melting temperature window ΔT_{pc}^* are defined as

$$T_{pc}^* = \frac{T_{pc} - T_{o,min}}{T_{o,max} - T_{o,min}} \quad \text{and} \quad \Delta T_{pc}^* = \frac{\Delta T_{pc}}{T_{o,max} - T_{o,min}}. \tag{11}$$

Here, the dimensionless latent heat of fusion h_{sf}^* is defined as

$$h_{sf}^* = \frac{\rho_{c+s} h_{sf}}{(\rho c_p)_{eff,s}(T_{o,max} - T_{o,min})}. \tag{12}$$

Additionally, the boundary conditions at the outer ($x^* = 0$) and inner ($x^* = 1$) wall surfaces given by Eq. (6) can be rewritten in dimensionless form as,

$$\frac{\partial T_w^*}{\partial x^*}(0, t^*) = -Bi_o[T_o^*(t^*) - T_w^*(0, t^*)] \quad \text{and}$$
$$\frac{\partial T_w^*}{\partial x^*}(1, t^*) = -Bi_i[T_w^*(1, t^*) - T_a^*(t^*)] \tag{13}$$

where $Bi_o = h_o/(Lk_{eff})$ and $Bi_i = h_i/(Lk_{eff})$ are the Biot numbers associated with the outside and inside convective thermal resistances, respectively.

Moreover, the energy conservation Eq. (4) for the inside temperature $T_a(t)$ can be non-dimensionalized by substituting the appropriate dimensionless variables of Eq. (8) to yield,

$$\frac{dT_a^*}{dt^*} = Bi_i C_r[T_w^*(1, t^*) - T_a^*(t^*)]. \tag{14}$$

Note that the product of dimensionless numbers Bi_i and C_r on the right side of Eq. (14) is defined as,

$$Bi_i C_r = \left(\frac{h_i L}{k_{eff}}\right)\left(\frac{(\rho c_p)_{eff,s} A_w L}{(\rho c_p)_a V_a}\right) \tag{15}$$

where C_r represents the ratio of the total heat capacity of the wall to that of the inside air.

Additionally, the sinusoidal outside temperature variation can be rewritten in dimensionless form by introducing a dimensionless oscillation period $\tau^* = \tau \alpha_{eff}/L^2$ representing the ratio of the oscillation period τ to the characteristic time for heat difffusion through

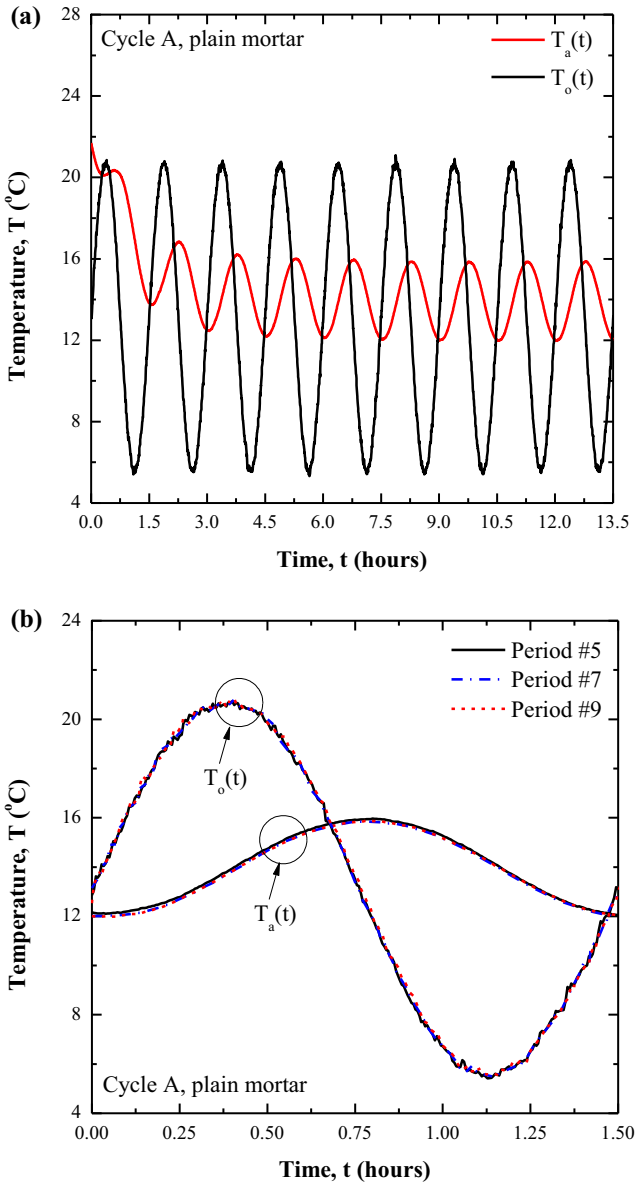

Fig. 3. (a) Experimentally measured chamber temperature $T_o(t)$ and inside air temperature $T_a(t)$ as functions of time t for a test cell with a plain mortar wall subjected to chamber temperature Cycle A. (b) Superimposed plots of $T_o(t)$ and $T_a(t)$ for the 5th, 7th, and 9th oscillation periods.

the wall L^2/α_{eff}. Then, the dimensionless outside temperature $T_o^*(t^*)$ can be expressed as,

$$T_o^*(t^*) = \frac{T_o(t) - T_{o,min}}{T_{o,max} - T_{o,min}} = 0.5\left[1 + \sin\left(\frac{2\pi t^*}{\tau^*}\right)\right]. \quad (16)$$

In summary, the seven dimensionless numbers $Bi_i, Bi_o, C_r, \tau^*, T_{pc}^*, \Delta T_{pc}^*$, and h_{sf}^* govern the behavior of $T_w(x,t)$ and $T_a(t)$. In practice, given two enclosures with different geometries and PCM phase change properties subjected to different sinusoidal outside temperature fluctuations, the transient dimensionless wall and inside air temperatures $T_w^*(x^*,t^*)$ and $T_a^*(t^*)$ will be identical provided that the dimensionless numbers $Bi_i, Bi_o, C_r, \tau^*, T_{pc}^*, \Delta T_{pc}^*$, and h_{sf}^* are identical.

This scaling analysis can be easily extended to situations when (i) solar radiation is incident on one or more faces of the envelope and (ii) heat is transferred through more than one wall.

5. Results and discussion

5.1. Verification of periodic steady-state

Fig. 3a plots the inside air temperature $T_a(t)$ experimentally measured as a function of time during Cycle A with a 1.5-h period for a test cell with a plain mortar wall panel. It also plots the imposed chamber temperature $T_o(t)$ as a function of time. In addition, Fig. 3b plots the 5th, 7th, and 9th periods of $T_a(t)$ and $T_o(t)$ for a test cell with a plain mortar wall. It is evident that the three cycles are superimposed on the same plot, establishing that the temperature $T_a(t)$ inside the test cell behaved periodically with the same frequency as that of $T_o(t)$ after 5 cycles. Then, the system had reached a periodic steady-state and the effect of the initial conditions vanished. Thus, for the remainder of this study, only a single oscillation period after the fifth cycle is considered.

5.2. Convective heat transfer coefficient estimation

In order to validate numerical predictions against experimental measurements, the model should use the convective heat transfer coefficients h_i and h_o prevailing experimentally. These parameters were estimated by finding the values of h_i and h_o that minimized the sum-of-squared error δ between the experimentally measured and numerically predicted inside air temperature over a single oscillation period, for a test cell subjected to Cycle A and with a plain mortar wall. The sum-of-squared error δ can be expressed as,

$$\delta = \sum_{k=1}^{N} (T_{a,exp}(t_k) - T_{a,num}(t_k))^2 \quad (17)$$

where $T_{a,exp}$ and $T_{a,num}$ are the inside air temperatures experimentally measured and numerically predicted at discrete times t_k, respectively. Here, N represents the number of time steps considered in a cycle. The resulting values for h_i and h_o that minimize δ for Cycle A were found to be 13 W/(m^2 K) and 20 W/(m^2 K), respectively.

5.3. Comparison between experiments and numerical simulations

Fig. 4 plots the experimentally measured and numerically predicted inside air temperature $T_a(t)$ and imposed outside temperature $T_o(t)$ for the test cell with either a plain mortar or a PCM-mortar composite wall over one oscillation period for (a-b) Cycle B, (c-d) Cycle C, and (e-f) Cycle D. Here, the experimentally measured minimum and maximum values of $T_o(t)$ were used as inputs to the numerical model. For all cycles, these values were about 0.6°C larger than the input values to the chamber temperature controller. Fig. 4 shows that, for Cycle B, the presence of PCM in the wall panel did not reduce the amplitude of the inside air temperature oscillations. Also, the presence of PCM did not delay the inside air temperature in reaching its maximum. Indeed, the outside temperature oscillated between 15 and 40 °C for Cycle B, while PCM melting/freezing took place between around 17 and 25 °C (Fig. 2). In these conditions, the temperature in most of the PCM-mortar wall remained above the melting temperature window. Thus, most of the PCM in the wall remained liquid. As a result, the increased thermal mass of the PCM wall during phase change was not exploited during this cycle.

On the other hand, Figs. 4c–f show a significant reduction in the amplitude of $T_a(t)$ for Cycles C and D when using a PCM-mortar composite wall panel compared with a plain mortar wall panel. Additionally, $T_a(t)$ reached its maximum at a later time for the PCM wall panel. This amplitude reduction and phase shift were due to melting and solidification of the PCM embedded in the wall.

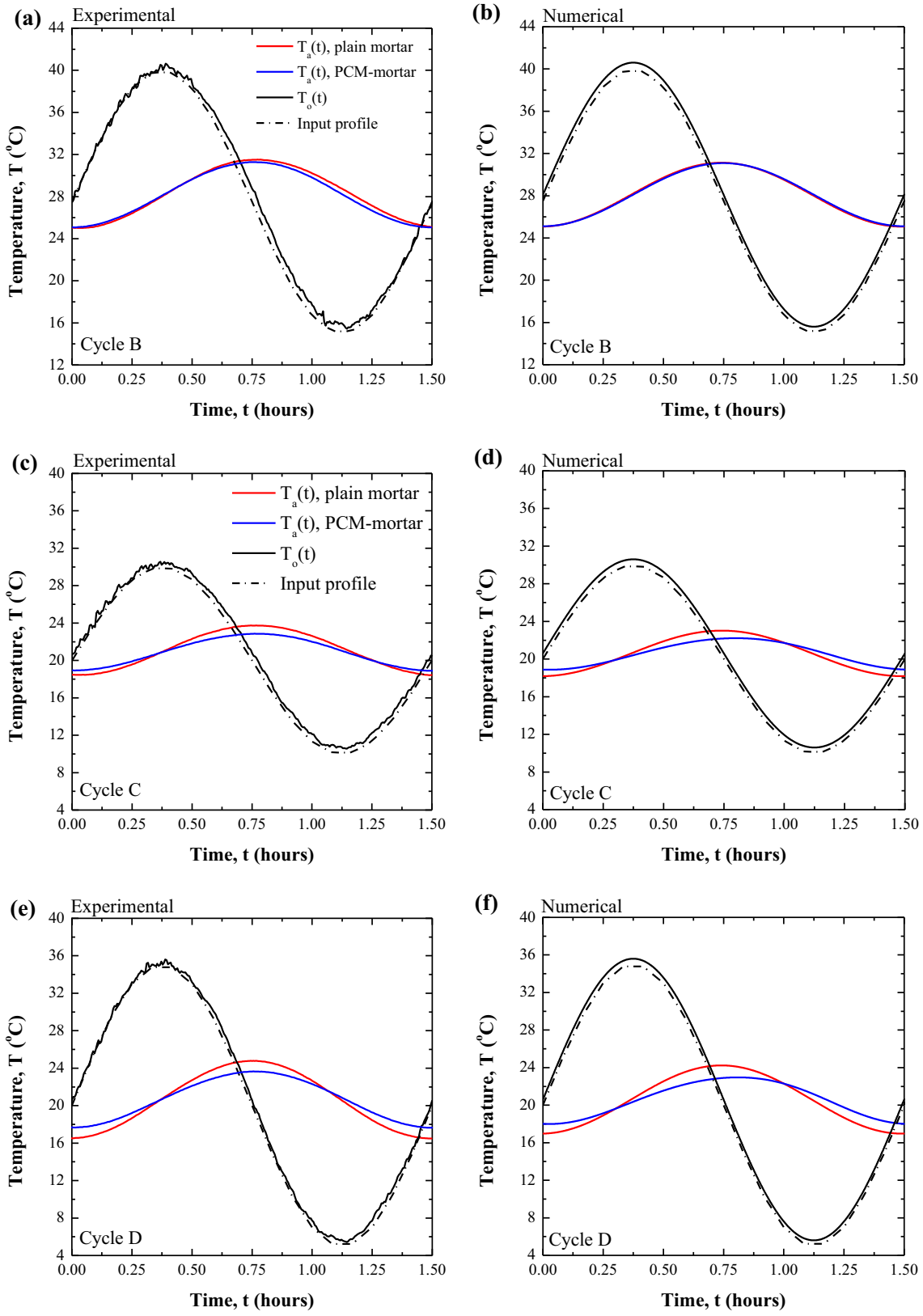

Fig. 4. Experimentally measured and numerically predicted inside air temperature $T_a(t)$ for test cells with either a plain mortar or PCM-mortar wall subjected to chamber temperature $T_o(t)$ corresponding to (a-b) Cycle B, (c-d) Cycle C, and (e-f) Cycle D.

In fact, $T_o(t)$ oscillated between 10 °C and 30 °C and between 5 °C and 35 °C for Cycles C and D, respectively, encompassing the PCM phase change temperature window of 17–25 °C.

Moreover, Fig. 4 shows good agreement between experimental measurements and numerical predictions. However, the effect of the PCM in delaying the maximum inside air temperature was

Table 2
Cases used for numerical validation of the scaling analysis. Case 1 corresponds to the experimental test cell subjected to chamber temperature Cycle C, while the other cases correspond to various full-scale enclosures. The values of the dimensionless numbers were, in all cases, Bi_o = 0.592, Bi_i = 0.278, C_r = 126, τ^* = 5.07, T^*_{pc} = 0.7, h^*_{sf} = 2.99, and ΔT^*_{pc} = 0.5.

Case	Type	L (m)	A_w (m^2)	V_a (m^3)	$T_{o,min}$ (°C)	$T_{o,max}$ (°C)	h_o (W/(m^2 K))	h_i (W/(m^2 K))	T_{pc} (°C)	ΔT_{pc} (°C)	h_{sf} (kJ/kg)	τ (h)
1	Small-scale	0.025	0.16	0.064	10	30	34	16	24	10	160	1.5
2	Large-scale #1	0.102	30	48	10	30	8.5	4	24	10	160	24
3		0.102	30	48	0	10	8.5	4	7	5	80	24
4		0.102	30	48	20	45	8.5	4	37.5	12.5	200	24
5	Large-scale #2	0.102	20	32	20	45	8.5	4	37.5	12.5	200	24
6		0.102	20	32	5	25	8.5	4	19	10	160	24
7		0.102	20	32	30	40	8.5	4	37	5	80	24
8	Medium-scale	0.072	10	11.31	15	35	12.02	5.66	29	10	160	12

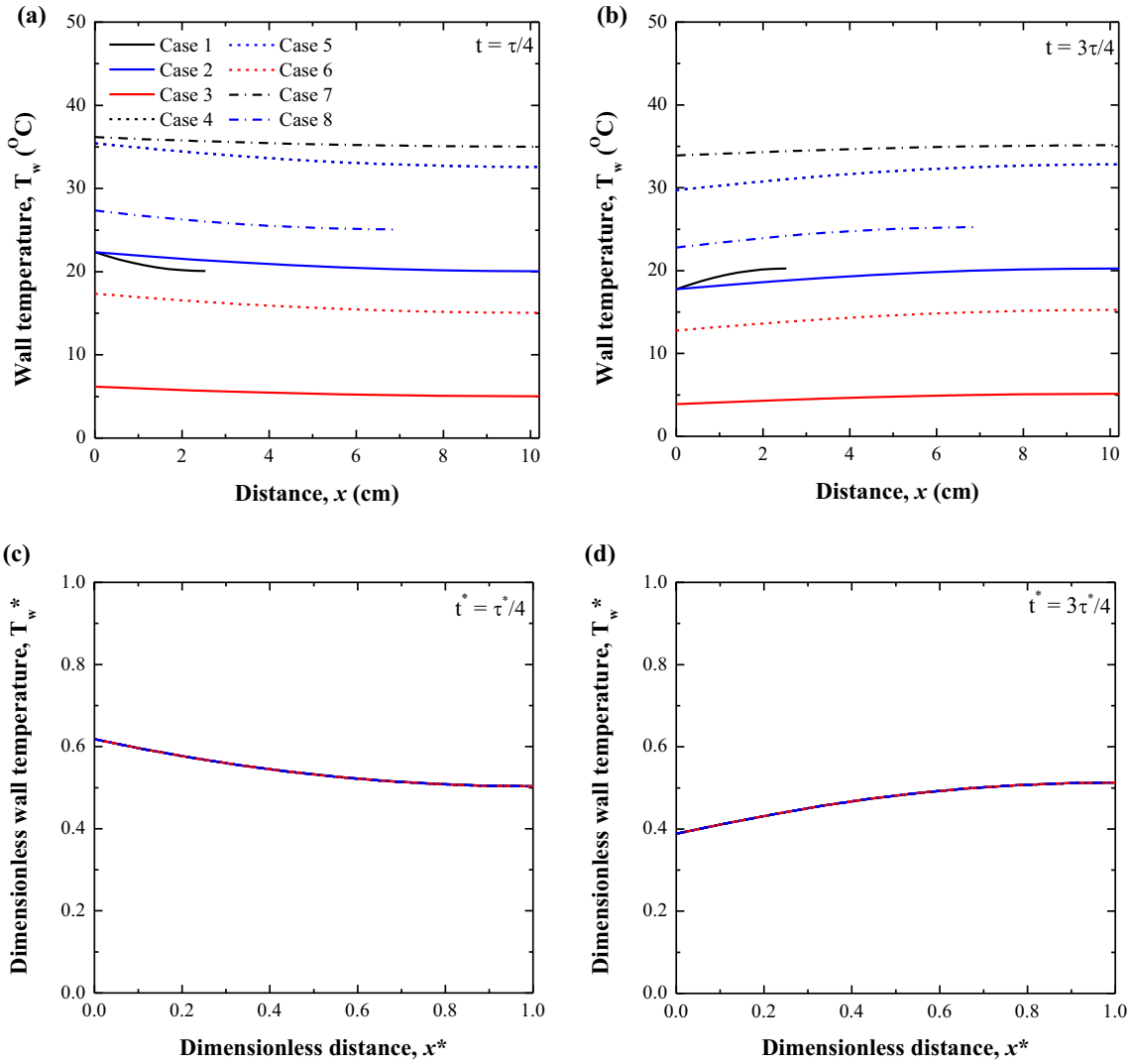

Fig. 5. Wall temperature $T_w(x,t)$ as a function of the spatial distance x for Cases 1–8 summarized in Table 2 shown at (a) $t = \tau/4$ and (b) $t = 3\tau/4$. Also shown is the dimensionless wall temperature $T^*_w(x^*,t^*)$ as a function of the dimensionless distance x^* for (c). $t^* = \tau^*/4$ and (d) $t^* = 3\tau^*/4$.

more pronounced in the numerical simulations than in the experiments. This discrepancy could be partially attributed to uncertainty in the material thermophysical properties used in the numerical model. In addition, both convective heat transfer coefficients h_i and h_o were treated as constants, while this may not be satisfied experimentally. Overall, Fig. 4 establishes that the numerical model could predict the thermal behavior of the test cells, with some minor discrepancies.

5.4. Scaling analysis

This section presents numerical validation of the scaling analysis. Here, the wall material considered was the composite PCM-mortar wall with 10 vol% PCM. For the purpose of scaling analysis and for parameterizing the problem, the temperature-dependent specific heat $c_{p,c+s}(T)$ of the microencapsulated PCM was estimated using the effective heat capacity method [Eq. (1)]. The PCM specific

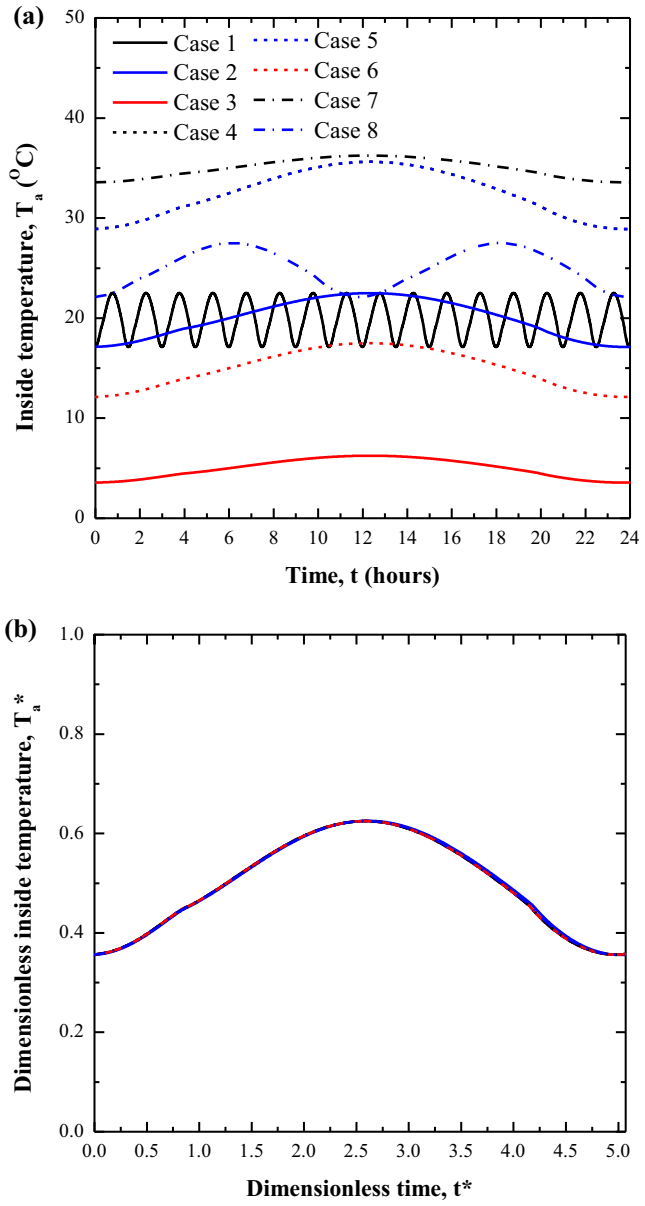

Fig. 6. (a) Inside temperature $T_a(t)$ as function of time t along with (b) dimensionless inside temperature $T_a^*(t^*)$ as a function of the dimensionless time t^* for Cases 1–8 summarized in Table 2.

heat outside the phase change temperature window was taken as $c_{p,c+s,s} = c_{p,c+s,l}$ = 1900 J/(kg K) [23]. Table 2 outlines several cases considering various values of (i) test cell dimensions, (ii) outside minimum $T_{o,min}$ and maximum $T_{o,max}$ temperatures, (iii) oscillation period τ, (iv) convective heat transfer coefficients h_o and h_i, (v) PCM melting temperature T_{pc}, (vi) PCM melting temperature window ΔT_{pc}, and (vii) latent heat of fusion h_{sf}. The values of the seven dimensionless numbers governing the temperatures in the wall and in the test cell were identical in all cases and equal to Bi_o = 0.592, Bi_i = 0.278, C_r = 126, τ^* = 5.07, T_{pc}^* = 0.7, ΔT_{pc}^* = 0.5, and h_{sf}^* = 2.99. The geometry of Case 1 corresponds to the reduced-scale experimental test cell presented previously and subjected to chamber temperature Cycle C with a period τ of 1.5 h. Cases 2–4 and Cases 5–7 represent two large-scale enclosures with different dimensions and a period τ of 24 h corresponding to actual outdoor diurnal cycles. Finally, Case 8 represents a medium-scale enclosure with a period of 12 h. The maximum $T_{o,max}$ and minimum $T_{o,min}$ outside temperatures were chosen to represent different climates. For example, Cases 3 and 4 correspond to a cold winter day and a hot summer day, respectively.

5.4.1. Wall temperature profiles

Figs. 5a and 5b plot the wall temperature $T_w(x,t)$ as a function of the distance x from the outer wall surface ranging from 0 to 0.102 m at time (a) $t = \tau/4$ and (b) $t = 3\tau/4$ for Cases 1–8 (Table 2). As expected, the temperature profiles at both times varied significantly among cases due to the differences in wall thickness, convective heat transfer coefficients, and outside temperatures. Figs. 5c and d plot the corresponding dimensionless wall temperature $T_w^*(x^*,t^*)$ as a function of the dimensionless distance $x^* = x/L$ ranging from 0 to 1 at dimensionless time t^* equals to $\tau^*/4$ and $3\tau^*/4$, respectively. It is evident that all the dimensionless temperature profiles at both times were identical for the eight cases considered. Similar results were obtained at any other time during the cycle. These results establish the validity of the scaling analysis for the wall temperature $T_w(x,t)$.

5.4.2. Inside air temperature

Fig. 6a plots the inside air temperature $T_a(t)$ as a function of time t ranging from 0 to 24 h for Cases 1–8 (Table 2). Here also, $T_a(t)$ varied significantly among cases due to the significant differences in dimensions, period τ, outdoor temperature $T_o(t)$, and PCM properties. Fig. 6b plots the dimensionless inside temperature $T_a^*(t^*)$ as a function of the dimensionless time t^* ranging from 0 to 5.07 corresponding to a single oscillation period. Once again, the dimensionless inside temperatures $T_a^*(t)$ collapsed on a single line for all cases considered.

Figs. 5 and 6 establish that scaling analysis of the experimentally-validated thermal model identified the seven dimensionless numbers governing the spatiotemporal behavior of $T_w(x,t)$ and $T_a(t)$. They indicate that the reduced-scale experimental test cell (Case 1) with a diurnal period of 1.5 h can be used to experimentally simulate the thermal behavior of large-scale enclosures (Cases 2–7 subjected to various daily outdoor temperature cycles.

5.5. Application to a real full-scale experimental setup

For illustration purposes, this section applies scaling analysis to two full-scale experimental outdoor 2 m × 2 m × 3 m cubicles with 12 cm-thick concrete walls constructed by Cabeza et al. [7]. In one cubicle, the north and east walls were made of plain concrete while the ceiling, south, and west walls were made of concrete with 5 wt% microencapsulated PCM. The PCM was reported to have latent heat h_{sf} = 110 kJ/kg and melting temperature T_{pc} = 26 °C [7]. The other cubicle was a reference structure for which all walls and ceiling were made of plain concrete. The cubicles were subjected to the outdoor environment of Lleida, Spain in the summer of 2005. Fig. 7a plots the outdoor temperature $T_o(t)$ and horizontal solar radiation flux $q''_{s,5}(t)$ as recorded during the experiment on June 6th, 2005 [7]. Here, the minimum and maximum outdoor temperatures were $T_{o,min} \approx 11$ °C and $T_{o,max} \approx 30$ °C.

Moreover, in simulating the experimental structures, the dimensionless energy conservation equation for the inside air given by Eq. (14) was modified to account for heat transfer through all four side walls and the ceiling such that,

$$\frac{dT_a^*}{dt^*} = \sum_{j=1}^{5} Bi_{i,j} C_{r,j} [T_{w,j}^*(1,t^*) - T_a^*(t^*)] \tag{18}$$

where the subscript j refers to the four walls and ceiling. Because the walls and ceiling had different compositions and boundary conditions, the dimensionless heat diffusion Eq. (9) for the wall temper-

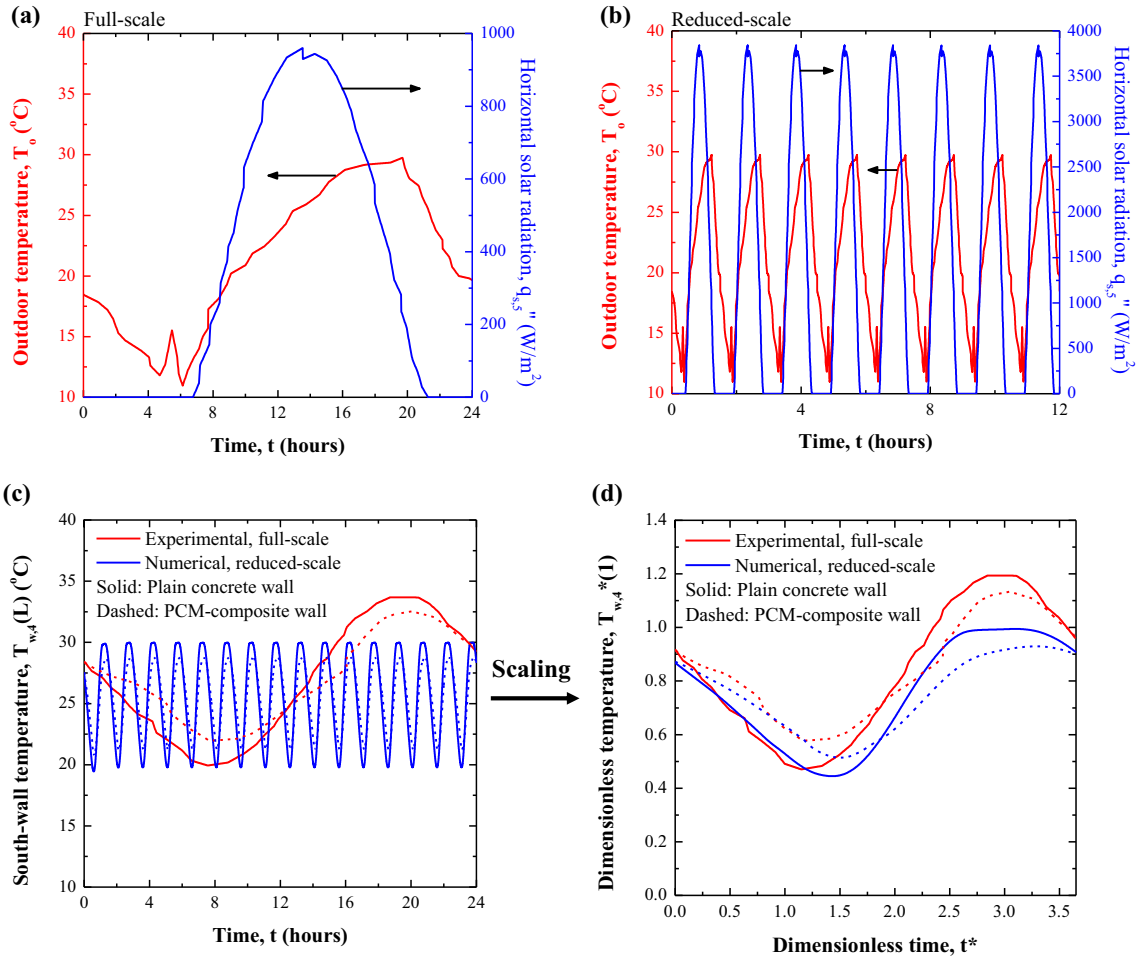

Fig. 7. (a) Outdoor temperature $T_o(t)$ and horizontal solar radiation flux $q''_{s,5}(t)$ corresponding to June 6th, 2005 in Lleida, Spain, measured by Cabeza et al. [7] during their experimental study of full-scale test cells with and without PCM-composite walls and (b) higher-frequency $T_o(t)$ and $q''_{s,5}(t)$ used as inputs to the reduced-scale numerical model. (c) South-wall temperature $T_{w,4}(L,t)$ and (d) dimensionless south-wall temperature $T^*_{w,4}(1,t^*)$ measured experimentally and predicted numerically using the reduced-scale model of the experimental structures.

Table 3
Thermal conductivity k, density ρ, and specific heat c_p used in numerical simulation of experiments conducted on full-scale cubicles by Cabeza et al. [7].

Material	Subscript	k (W/(m K))	ρ (kg/m^3)	c_p (J/(kg K))	Ref.
Concrete	m	1.4	2300	880	[21]
PCM	c	0.21	900	1900	[23]
Melamine-formate (MF)	s	0.42	1500	1670	[29]

Table 4
Parameters corresponding to the experimental cubicles studied by Cabeza et al. [7] and those corresponding to a reduced-scale model with identical dimensionless numbers $Bi_{o,j}, Bi_{i,j}, C_{r,j}, \tau_j, T^*_{pc}, \Delta T^*_{pc}, h^*_{sf}$, and $q''^*_{s,j}(t^*)$.

Type	L (m)	Width (m)	Depth (m)	Height (m)	h_o (W/(m^2 K))	h_i (W/(m^2 K))	τ (hr)
Experimental [7]	0.12	2	2	3	10	7.7	24
Reduced-scale	0.03	0.5	0.5	0.75	40	30.8	1.5

atures $T^*_{w,j}(x^*,t^*)$ was solved for each wall separately. In addition, the boundary condition at each outer wall surface, given by Eq. (13), was modified to include the effect of the incident solar radiation flux $q''_{s,j}(t)$, i.e.,

$$\frac{\partial T^*_{w,j}}{\partial x^*}(0,t^*) = -Bi_{o,j}[T^*_o(t^*) - T^*_{w,j}(0,t^*)] - \alpha_s q''^*_{s,j}(t^*) \tag{19}$$

where the dimensionless solar radiation flux $q''^*_{s,j}(t^*)$ was defined as,

$$q''^*_{s,j}(t^*) = \frac{q''_{s,j}(t)L_j}{k_{eff,j}(T_{o,max} - T_{o,min})}. \tag{20}$$

Here, incident solar radiation was ignored except on the ceiling ($j = 5$) and south wall ($j = 4$), i.e., $q''_{s,j}(t) = 0$ for $j \in \{1,2,3\}$. The following relationship was used to estimate the solar radiation flux on the south wall $q''_{s,4}(t)$ using the experimentally measured solar radiation flux on the horizontal ceiling $q''_{s,5}(t)$ [24],

$$\frac{q''_{s,4}(t)}{q''_{s,5}(t)} = \frac{\cos\theta_e(t)\cos(180^\circ - \theta_a(t))}{\sin\theta_e(t)} \tag{21}$$

where $\theta_e(t)$ and $\theta_a(t)$ are the elevation and azimuthal angles of the sun, respectively. They depend on the time of day, the geographic latitude $\Phi = 41^\circ$N, and the day number d (= 157 for June 6th).

Table 3 summarizes the thermophysical properties of the concrete, shell, and PCM used in the simulations. The PCM melting temperature window ΔT_{pc} was taken as 8 °C based on experimental measurements of similar PCMs [18]. Note that the shell material used experimentally was not specified. In the simulation the shell was assumed to be made of melamine-formate (MF), as used commercially [19]. The effective thermal conductivity k_{eff} of the PCM-composite walls was estimated using the Felske model [15] while the effective volumetric heat capacity $(\rho c_p)_{eff}$ was again determined using a volume-weighted average. The composition of the PCM microcapsules was assumed to be such that $\phi_c/(\phi_c + \phi_s)$ = 0.85. Based on the density ρ_c = 900 kg/m^3 given in Table 3 and the wt% reported in Ref. [7], the core and shell volume fractions were estimated as ϕ_c = 0.102 and ϕ_s = 0.018. The indoor convective heat transfer coefficient h_i was taken as 7.7 W/(m^2 K) based on the ISO standard [25]. The outdoor convective heat transfer coefficient h_o was estimated using the correlation developed by Defraeye et al. [26] for a leeward exterior building wall given by,

$$h_o = 2.27U_\infty^{0.83} \tag{22}$$

where U_∞ is the wind speed (in m/s) and h_o is in W/(m^2 K). Here, U_∞ was taken as 6 m/s based on the average value for a summer in the region of Lleida [27], resulting in h_o = 10.0 W/(m^2 K). Note that the actual value of h_o prevailing experimentally would vary with time based on the speed and direction of the wind. The wind speed reported by Cabeza et al. [7] on a different day fluctuated between 0 and 20 m/s, but featured an average value of less than 10 m/s. Finally, the total hemispherical solar absorptivity of the wall surfaces α_s was taken as 0.6 corresponding to unpainted concrete [21].

Table 4 summarizes the dimensions, convective heat transfer coefficients h_o and h_i, and oscillation period τ corresponding to the experimental setup used in Ref. [7] as well as those for the equivalent reduced-scale model. The dimensions of the reduced-scale model were chosen such that the dimensionless numbers $Bi_{i,j}, Bi_{o,j}$, and $C_{r,j}$ for each wall were identical to those estimated for the outdoor building structures. Specifically, the Biot numbers for the PCM-composite side walls ($j \in \{3,4\}$) and ceiling ($j = 5$) were $Bi_{i,3\leqslant j\leqslant 5}$ = 0.76 and $Bi_{o,3\leqslant j\leqslant 5}$ = 0.99. They were of the same order of magnitude as those reported for our experimental apparatus discussed previously in Section 3. Likewise, the values of $C_{r,3\leqslant j\leqslant 4} = 99.5$ for the PCM-composite side walls and $C_{r,5} = 66.4$ for the ceiling were similar in magnitude to C_r = 126 for our test cell. The plain concrete walls ($j \in \{1,2\}$) had $Bi_{i,1\leqslant j\leqslant 2} = 0.66, Bi_{o,1\leqslant j\leqslant 2} = 0.85$, and $C_{r,1\leqslant j\leqslant 2} = 100.7$. On the other hand, the values of $T_{pc}, \Delta T_{pc}$, and $h_{sf}, T_{o,min}$, and $T_{o,max}$ were the same for the reduced-scale model as for the full-scale experiment, and such that T^*_{pc} = 0.79, ΔT^*_{pc} = 0.42, and h^*_{sf} = 2.6 in both cases. Finally, the dimensionless period τ^* based on the thermal diffusivity of the PCM-composite walls was equal to 3.64 in both cases.

The measured outdoor temperature $T_o(t)$ and solar irradiation $q''_{s,5}(t)$ in the full-scale setup of Ref. [7] were scaled to have an oscillation period τ = 1.5 h in the reduced-scale model, as illustrated in Fig. 7b. Additionally, the magnitude of the imposed solar radiation flux on both the roof and south wall was scaled such that the dimensionless radiation flux $q''^*_{s,j}(t^*)$ given by Eq. (20) was identical for both cases. These scaled profiles were used as the boundary conditions for the reduced-scale model.

Fig. 7c plots the interior (i.e., $x = L$) south-wall temperature $T_{w,4}(L,t)$ as a function of time t ranging from 0 to 24 h measured experimentally [7] and predicted numerically using the previously described reduced-scale model for structures with and without PCM-composite walls. Additionally, Fig. 7d plots the corresponding dimensionless interior (x^* = 1) south-wall surface temperature $T^*_{w,4}(1,t^*)$ as a function of dimensionless time t^* over one oscillation period. It shows good agreement between the values of $T^*_{w,4}(1,t^*)$ measured experimentally and those predicted numerically. The underprediction of the maximum value of $T^*_{w,4}(1,t^*)$ can be attributed to uncertainty in (i) the wall material properties, (ii) the experimental outdoor convective heat transfer coefficient h_o, and (iii) a possible underprediction of the south wall solar radiation flux. However, the effect of PCM in reducing the magnitude of the inner south-wall temperature fluctuation was accurately captured by the scaled model.

These results illustrate the ability of scaling analysis to represent the thermal behavior of a realistic full-scale structure with a reduced-scale model. Therefore, rather than constructing a full-scale structure to evaluate the thermal performance of various building envelope materials, including those containing PCM, one could simply determine the eight dimensionless numbers governing the thermal behavior of the building envelope, and then design a reduced-scale model with identical dimensionless numbers to be conveniently tested in a laboratory environmental chamber.

6. Conclusion

This study presented an approach to experimentally evaluate the performance of PCM-composite building envelope materials without requiring a significant amount of time, material, or space. First, a transient thermal model accounting for the thermal coupling between PCM-composite wall and inside air temperatures of an enclosure was outlined. Then, the thermal model was validated against experimental temperature measurements on a reduced-scale test cell subjected to sinusoidal outdoor temperature oscillations. Scaling analysis of coupled energy conservation equations and their boundary conditions was developed and identified seven (eight if accounting for incident solar radiation) relevant dimensionless numbers governing the thermal behavior of the test cell including melting and solidification of the PCM. This scaling analysis was validated with a previously developed numerical simulation tool. The application of the scaling analysis to experimental results from a full-scale outdoor structure [7] was then illustrated. The results demonstrated that a full-scale enclosure exposed to a realistic outdoor climate can be represented by a reduced-scale test cell in an environmental chamber.

Acknowledgments

This manuscript was prepared as a result of work sponsored by the California Energy Commission (Contract: PIR:-12-032), the National Science Foundation (CMMI: 1130028) and the University of California, Los Angeles (UCLA). It does not necessarily represent the views of the Energy Commission, its employees, the State of California, or the National Science Foundation. The Energy Commission, the State of California, its employees, contractors, and subcontractors make no warranty, expressed or implied, and assume no legal liability for the information in this document; nor does any party represent that the use of this information will not infringe upon privately owned rights. This manuscript has not been approved or disapproved by the California Energy Commission nor has the California Energy Commission passed upon the accuracy or adequacy of the information in this paper.

References

[1] U.S. Department of Energy, Buildings Energy Data Book, D&R International, Silver Spring, Maryland, 2015.
[2] A.M. Khudhair, M.M. Farid, A review on energy conservation in building applications with thermal storage by latent heat using phase change materials, Energy Convers. Manage. 45 (2) (2004) 263–275.
[3] F. Kuznik, D. David, K. Johannes, J. Roux, A review on phase change materials integrated in building walls, Renew. Sustain. Energy Rev. 15 (1) (2011) 379–391.
[4] M.M. Farid, A.M. Khudhair, S.A.K. Razack, S. Al-Hallaj, A review on phase change energy storage: materials and applications, Energy Convers. Manage. 45 (9) (2004) 1597–1615.
[5] L.F. Cabeza, A. Castell, C. Barreneche, A. De Gracia, A.I. Fernández, Materials used as PCM in thermal energy storage in buildings: a review, Renew. Sustain. Energy Rev. 15 (3) (2011) 1675–1695.
[6] A.M. Thiele, A. Kumar, G. Sant, L. Pilon, Effective thermal conductivity of three-component composites containing spherical capsules, Int. J. Heat Mass Transfer 73 (2014) 177–185.
[7] L.F. Cabeza, C. Castellon, M. Nogues, M. Medrano, R. Leppers, O. Zubillaga, Use of microencapsulated PCM in concrete walls for energy savings, Energy Build. 39 (2) (2007) 113–119.
[8] A. Castell, I. Martorell, M. Medrano, G. Pérez, L.F. Cabeza, Experimental study of using PCM in brick constructive solutions for passive cooling, Energy Build. 42 (4) (2010) 534–540.
[9] M. Zhang, M.A. Medina, J.B. King, Development of a thermally enhanced frame wall with phase-change materials for on-peak air conditioning demand reduction and energy savings in residential buildings, Int. J. Energy Res. 29 (9) (2005) 795–809.
[10] F. Kuznik, J. Virgone, Experimental assessment of a phase change material for wall building use, Appl. Energy 86 (10) (2009) 2038–2046.
[11] X. Fang, Z. Zhang, A novel montmorillonite-based composite phase change material and its applications in thermal storage building materials, Energy Build. 38 (4) (2006) 377–380.
[12] B. Delcroix, M. Kummert, A. Daoud, J. Bouchard, Experimental assessment of a phase change material in walls for heating and cooling applications, in: Proceedings of eSim, International Building Performance Simulation Association, Ottawa, Canada, May 8–9, 2014.
[13] A.M. Thiele, G. Sant, L. Pilon, Diurnal thermal analysis of microencapsulated PCM-concrete composite walls, Energy Convers. Manage. 93 (2015) 215–227.
[14] A. Ricklefs, A.M. Thiele, G. Falzone, G. Sant, L. Pilon, Thermal conductivity of cementitious composites containing microencapsulated phase change materials, Int. J. Heat Mass Transfer 104 (2017) 72–82.
[15] J.D. Felske, Effective thermal conductivity of composite spheres in a continuous medium with contact resistance, Int. J. Heat Mass Transfer 47 (14) (2004) 3453–3461.
[16] ASTM Standard, E1269-11, Standard test method for determining specific heat capacity by differential scanning calorimetry. ASTM International, West Conshohocken, PA, USA, 2011.
[17] S.N. Al-Saadi, Z.J. Zhai, Modeling phase change materials embedded in building enclosure: a review, Renew. Sustain. Energy Rev. 21 (2013) 659–673.
[18] A.M. Thiele, Z. Wei, G. Falzone, B.A. Young, N. Neithalath, G. Sant, L. Pilon, Figure of merit for the thermal performance of cementitious composites containing phase change materials, Cem. Concr. Compos. 65 (2016) 214–226.
[19] MPCM Technical Information, Tech. Rep., Microtek Laboratories Inc., Dayton, OH.
[20] ASTM Standard, "C305", Standard practice for mechanical mixing of hydraulic cement pastes and mortars of plastic consistency, ASTM International, West Conshohocken, PA, USA, 2014.
[21] T.L. Bergman, A.S. Lavine, F.P. Incropera, D.P. DeWitt, Fundamentals of Heat and Mass Transfer, seventh ed., John Wiley & Sons, New York City, NY, 2011.
[22] W. Ogoh, D. Groulx, Stefan's problem: validation of a one-dimensional solid-liquid phase change heat transfer process, in: Proceedings of the COMSOL Conference, COMSOL Inc, Boston, MA, October 7–9, 2010.
[23] N. Ukrainczyk, S. Kurajica, J. Šipušić, Thermophysical comparison of five commercial paraffin waxes as latent heat storage materials, Chem. Biochem. Eng. Q. 24 (2) (2010) 129–137.
[24] J.E. Braun, J.C. Mitchell, Solar geometry for fixed and tracking surfaces, Sol. Energy 31 (5) (1983) 439–444.
[25] EN ISO, "6946", Building components and building elements: thermal resistance and thermal transmittance calculation method, International Organization for Standardization, Oslo, Norway, 1996.
[26] T. Defraeye, B. Blocken, J. Carmeliet, Convective heat transfer coefficients for exterior building surfaces: existing correlations and CFD modelling, Energy Convers. Manage. 52 (1) (2011) 512–522.
[27] J. Diebel, J. Norda, Weatherspark, Cedar Lake Ventures Inc, 2013.
[28] D.P. Bentz, Transient plane source measurements of the thermal properties of hydrating cement pastes, Mater. Struct. 40 (10) (2007) 1073–1080.
[29] R.K. Rajput, Engineering Materials & Metallurgy, first ed., S. Chand Limited, New Delhi, India, 2006.